J. Plasma Phys. (2026), *vol*. 92, E59 © The Author(s), 2026. Published by Cambridge University Press. This is an Open Access article, distributed under the terms of the Creative Commons Attribution licence (https://creativecommons.org/licenses/by/4.0/), which permits unrestricted re-use, distribution and reproduction, provided the original article is properly cited.
doi:10.1017/S0022377826101603

Assessing parametric instabilities of trapped microwaves in full spatio-temporal framework

J.K. de Wit[1], A. Clod[1], M.G. Senstius[2] and S.K. Nielsen[1]

[1]Department of Physics, Technical University of Denmark, Fysikvej, DK-2800 Kongens Lyngby, Denmark

[2]United Kingdom Atomic Energy Authority, Culham Science Centre, Abingdon OX14 3DB, UK

Corresponding author: J.K. de Wit, johdew@dtu.dk

(Received 14 December 2025; revision received 20 February 2026; accepted 6 March 2026)

The two-plasmon decay instability of high-power microwaves used for electron cyclotron resonance heating has been observed experimentally in multiple fusion devices. This type of instability is a nonlinear three-wave interaction that can transfer energy away from the cyclotron harmonics. Analytical models quantify exponential growth rates and power thresholds, but typically evaluate the growth as a spatially averaged gain over the interaction region of the instability. This description effectively excludes field inhomogeneities and noise, leaving their impact on the instability growth uncertain. We assess this assumption by solving the full nonlinear system on a spatial grid. Across all cases considered, we find that the instabilities drive the wave fields toward the spatially averaged behaviour. After a transient period that scales inversely with the instability growth rate, the simulated growth converges to the averaged prediction, indicating that the established models are asymptotically valid.

Key words: plasma instabilities, two-plasmon decay instability, electron Bernstein wave, plasma heating

1. Introduction

In recent decades, a large effort has been devoted to understanding the two-plasmon decay instability (TPDI) of injected high-power microwaves in magnetically confined fusion devices. Signatures of this instability have been observed for injected X-mode waves used for second harmonic electron cyclotron resonance heating (ECRH) in both tokamaks and stellarators (Westerhof *et al*. 2009; Nielsen *et al*. 2013; Hansen *et al*. 2020; Tancetti *et al*. 2022*a*,*b*; Clod *et al*. 2024). In these cases, the injected X-mode wave traversed a non-monotonic plasma perturbation in which thermally excited upper hybrid (UH) waves propagate. The UH waves can be trapped in the perturbation due to linear mode conversion between X-mode waves and backward-propagating electron Bernstein waves (EBWs) at UH layers that surround the perturbation.

As the injected ECRH wave propagate through the structure, it can couple parametrically into a pair of trapped UH waves, resulting in a transfer of energy between

the three waves (Popov & Gusakov 2015). The trapping mechanism created by the plasma profile reduces the convection losses of the UH waves. This causes the UH waves to grow exponentially in time from the instability once the power threshold is exceeded. At higher amplitudes the UH waves saturate through further parametric decays, leading to a more complicated system of coupled waves. Analytical studies predict that the energy drained by the UH waves can reach up to 80 % of the injected wave (Gusakov & Popov 2016, 2017; Gusakov *et al*. 2019*a*). The instability is therefore predicted to potentially alter the heating profile, ultimately reducing the efficiency of the ECRH scheme.

In the analytical models, the exponential growth is evaluated as a spatially averaged gain over the interaction region of the instability (Gusakov & Popov 2016; Senstius *et al*. 2022; Clod *et al*. 2024). This allows for a more convenient numerical evaluation, but prohibits local inhomogeneities and noise from being included in the description of the trapped UH waves. Instead, the daughter wave fields are described using a separation of variables, consisting of a time-dependent component and a spatially dependent one (Hansen 2019; Clod *et al*. 2024).

The impact of this approximation on the instability growth is uncertain and, to assess it, we solve the envelope equation from geometrical optics (Tracy *et al*. 2014; Dodin *et al*. 2019) on a spatial grid. The system is then evolved forward in time with a fourth-order Runge–Kutta scheme where the daughter waves are also influenced by the nonlinear growth of the TPDI. For comparison with the spatially averaged model, and to test the linear evolution of the waves, the wave fields are initialised with large inhomogeneities and noise.

We find that the UH wave amplitudes evolve toward a time-independent spatial profile multiplied by an exponential growth in time. Convergence is reached after a transient period inversely proportional to the growth rate of the instability. In this regime, the amplitudes are consistent with the wave field description assumed in the spatially averaged models. The computed growth rates here agree closely with those obtained by the spatially averaged description as well. This indicates that the analytical assumptions in the spatially averaged models capture the essential physics of the TPDI asymptotically.

2. Theory

2.1. *Dispersion relations of EBWs and X-mode*

We investigate the TPDI between an injected X-mode polarised wave and two trapped UH waves. The UH waves have frequencies close to but below the UH frequency, and they consist of both an EBW and X-mode component. In this section, we outline the dispersion relations used to obtain the frequencies and wavenumbers of the injected X-mode and the two UH waves. The TPDI requires conservation of energy and momentum among the three waves, which manifest as the resonance conditions for the instability

$$\begin{aligned} \omega_0 &= \omega_1 + \omega_2, \\ \boldsymbol{k}_0 &= \boldsymbol{k}_1 + \boldsymbol{k}_2, \end{aligned} \tag{2.1}$$

where ω is the angular frequency and $\boldsymbol{k}$ is the wave vector. The subscript 0 is the injected pump wave, and 1, 2 are the two UH daughter waves. To align with previous numerical studies of the TPDI (Senstius *et al*. 2019, 2022; de Wit *et al*. 2025), the system is confined to a one-dimensional geometry along the x-axis. The EBWs propagate almost perfectly perpendicular to the magnetic field, and we therefore choose the magnetic field to point completely in the z-direction such that $\boldsymbol{B} = B^{(0)}\hat{\boldsymbol{z}}$,

https://doi.org/10.1017/S0022377826101603 Published online by Cambridge University Press

where $B^{(0)}$ is the magnetic field strength. The general kinetic dispersion relation for linear waves in a magnetised plasma is given as (Swanson 2003)

$$\begin{aligned}&\left[\gamma\left(\gamma-\kappa_0+k_\perp^2\right)+\kappa_2^2\right]\kappa_3+k_\perp^2\left[\left(\gamma-\kappa_0+k_\perp^2\right)\kappa_1-\kappa_2^2\right]\\&+\kappa_4\left(\gamma-\kappa_0+k_\perp^2\right)\left(2k_\perp k_\parallel+\kappa_4\right)\\&-\kappa_5\left[\gamma\kappa_5+2\kappa_2\left(k_\perp k_\parallel+\kappa_4\right)\right]=0,\end{aligned}\tag{2.2}$$

where $\gamma=k_\parallel^2-\kappa_1$, and $\kappa_i=\omega^2/c^2K_i$. The speed of light in vacuum is c, the parallel and perpendicular components of the wave vector are $k_\parallel$, $k_\perp$, respectively, and the ith dielectric tensor element is K_i. In the limit of $k_\parallel=0$, the dispersion relation reduces to

$$\mathcal{D}=\left(\kappa_3-k_\perp^2\right)\left(\kappa_1\left[\kappa_0+\kappa_1-k_\perp^2\right]+\kappa_2^2\right)=0,\tag{2.3}$$

and the dielectric tensor elements become (Clod *et al*. 2025)

$$K_0=-2\sum_\sigma\frac{\omega_{p\sigma}^2}{\omega}\lambda_\sigma e^{-\lambda_\sigma}\sum_{n=-\infty}^{\infty}\frac{I_n(\lambda_\sigma)-I_n'(\lambda_\sigma)}{\omega-n\omega_{c\sigma}},\tag{2.4}$$

$$K_1=1-\sum_\sigma\frac{\omega_{p\sigma}^2}{\omega}\frac{e^{-\lambda_\sigma}}{\lambda_\sigma}\sum_{n=-\infty}^{\infty}\frac{n^2I_n(\lambda_\sigma)}{\omega-n\omega_{c\sigma}},\tag{2.5}$$

$$K_2=-i\sum_\sigma\frac{\mathrm{sgn}(q_\sigma)\,\omega_{p\sigma}^2}{\omega}e^{-\lambda_\sigma}\sum_{n=-\infty}^{\infty}\frac{n[I_n(\lambda_\sigma)-I_n'(\lambda_\sigma)]}{\omega-n\omega_{c\sigma}},\tag{2.6}$$

$$K_3=1-\sum_\sigma\frac{\omega_{p\sigma}^2}{\omega}e^{-\lambda_\sigma}\sum_{n=-\infty}^{\infty}\frac{I_n(\lambda_\sigma)}{\omega-n\omega_{c\sigma}},\tag{2.7}$$

with $\omega_{p\sigma}^2=q_\sigma^2n_\sigma/(\varepsilon_0m_\sigma)$ and $\omega_{c\sigma}=|q_\sigma|B^{(0)}/m_\sigma$ being the angular plasma frequency and angular cyclotron frequency of species $\sigma\in\{\text{electrons, ions}\}$, respectively. The mass of species σ is m_σ, the vacuum permittivity is ε_0, the charge is q_σ, and the number density is n_σ. The modified Bessel function of the first kind of order n is given as I_n, where I_n' is its derivative. Their arguments are $\lambda_\sigma=k^2\rho_{L\sigma}^2/2$, where $\rho_{L\sigma}=\omega_{c\sigma}/v_{t\sigma}$ is the Larmor radius. The thermal velocity of species σ is defined as $v_{t\sigma}^2=2T_\sigma/m_\sigma$, with T_σ being the temperature in units of energy.

The first solution in (2.3) of $\kappa_3=k_\perp^2$ describes the ordinary mode polarisation (Clod *et al*. 2025). The second bracket in (2.3) instead yields dispersion relation for the three waves

$$\begin{aligned}&\kappa_1\left[\kappa_0+\kappa_1-k_\perp^2\right]+\kappa_2^2=0\Rightarrow\\&\mathcal{D}=k_\perp^2K_1-\frac{\omega^2}{c^2}\left(K_0K_1+K_1^2+K_2^2\right)=0.\end{aligned}\tag{2.8}$$

The first term on the right-hand side in (2.8) is recognised as the contribution from the electrostatic dispersion relation (Swanson 2003), and the second term includes the electromagnetic response. The kinetic framework is essential for describing the resonant coupling between the waves and the collective cyclotron motion of the plasma species. However, away from the resonances, the electromagnetic effects are typically sufficiently modelled using the cold plasma limit

$$\lim_{T\to0}\left\{\frac{\omega^2}{c^2}\left(K_0K_1+K_1^2+K_2^2\right)\right\}=\frac{\omega^2}{c^2}(S^2-D^2),\tag{2.9}$$

https://doi.org/10.1017/S0022377826101603 Published online by Cambridge University Press

where S and D are the sum and difference Stix parameters

$$S = 1 - \sum_{\sigma} \frac{\omega_{p\sigma}^2}{\omega^2 - \omega_{c\sigma}^2}, \qquad D = \sum_{\sigma} \frac{\omega_{c\sigma}}{\omega} \frac{\mathrm{sgn}(q_\sigma)\omega_{p\sigma}^2}{\omega^2 - \omega_{c\sigma}^2}. \tag{2.10}$$

The resulting dispersion relation for the two UH daughter waves of the TPDI becomes

$$\mathcal{D} = k^2 K_1 - \frac{\omega^2}{c^2}(S^2 - D^2) = 0, \tag{2.11}$$

where k is understood as the perpendicular component $k_\perp$. The expression in (2.11) has previously been used in multiple TPDI studies such as in Hansen *et al*. (2023), Clod *et al*. (2024), Senstius, Freethy & Nielsen (2024) and Clod *et al*. (2025). For the injected X-mode wave, the complete cold limit of (2.11) is sufficient. Letting $\lim_{T\to 0} K_1 = S$, the known dispersion relation for the X-mode polarisation from cold plasma theory is obtained (Swanson 2003):

$$k_0^2 = \sum_{\sigma} \frac{1}{c^2}\left(\omega^2 - \omega_{p\sigma}^2 \frac{\omega^2 - \omega_{p\sigma}^2}{\omega^2 - \omega_{UH}^2}\right), \tag{2.12}$$

where $\omega_{UH}^2 = \omega_{pe}^2 + \omega_{ce}^2$ is the characteristic angular UH frequency.

2.2. *The plasma profile*

The two UH waves are confined by a mode conversion between their X-mode and EBW components at the UH layers of the plasma profile. The plasma parameters are selected such that UH layers for the two UH waves are located on opposite ends of the profile. The number density, magnetic field strength, and temperature are symmetric around 0.5 and are shown in the top panel of figure 1. A previous study of de Wit *et al*. (2025) investigated the TPDI in plasma conditions that were achievable in smaller-scale plasma devices, where the growth rate estimations showed a reasonable agreement with particle-in-cell simulations across a wide range of plasma parameters. Similar plasma conditions are chosen for this study, and the frequency of the X-mode pump wave is set to $\omega_0/(2\pi) = 5.8\,\mathrm{GHz}$. This causes the central plasma parameters of $n_0 = 3.44 \times 10^{16}\,\mathrm{m}^{-3}$, $B_0 = 0.09\,\mathrm{T}$, $T_0 = 5\,\mathrm{eV}$ and $x_{\mathrm{end}} = 10\,\mathrm{cm}$ to support the trapping mechanism of the daughter waves, and thus enable the TPDI.

We consider daughter waves which satisfy the resonance conditions at the centre of the profile, causing their frequencies to become $\omega_1/(2\pi) \approx 2.897\,\mathrm{GHz}$ and $\omega_2/(2\pi) \approx 2.903\,\mathrm{GHz}$. Their resulting wavenumbers are shown as a function of position in the lower panel of figure 1, where they are plotted in such a way that the overlap of the lines marks $k_0 = k_1 + k_2$, thereby satisfying the resonance conditions.

2.3. *Growth rate estimation*

It is typically the EBW components of the UH waves that couple most strongly to the injected X-mode wave due to their low group velocity and comparatively high electric field amplitudes. We therefore select the plasma parameters to fulfil the phase matching condition between these components of the UH waves and consider them only in the three-wave interaction for the TPDI. Furthermore, the

https://doi.org/10.1017/S0022377826101603 Published online by Cambridge University Press

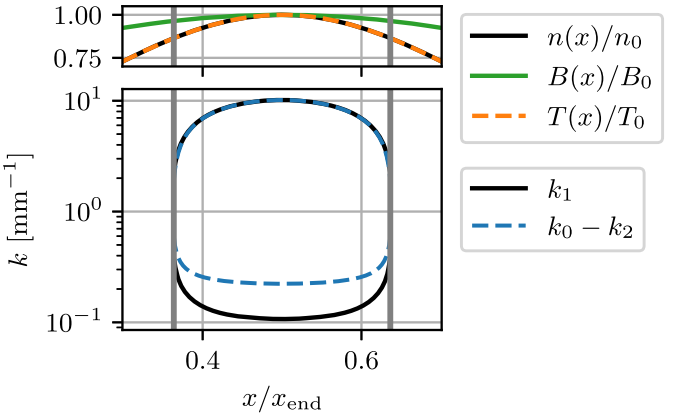


FIGURE 1. Top panel: the plasma parameters as a function of x. The black and orange lines show the number density and temperature of electrons, respectively, and the green line is the background magnetic field. All quantities are normalised by their central values. Lower panel: the wavenumbers of the three waves as a function of position. The grey lines on both panels show the location of the UH layers.

UH frequency is close to the frequency of the UH waves throughout the whole plasma profile, causing their X-mode components to be mostly longitudinal as well. The system is on account of this approximated as fully electrostatic, and the starting point is the non-local dispersion relation, with a source term added due to nonlinear wave interactions (Hansen 2019)

$$\frac{\rho_{\mathrm{nl}}(x,t)}{\varepsilon_0} = \int_{\mathrm{all}\ (x',t')} \mathcal{D}(x',t',x,t)\ \Phi(x',t')\ \mathrm{d}x'\mathrm{d}t'. \tag{2.13}$$

The nonlinear charge density induced by the TPDI is ρ_{nl}, and the dispersion kernel is $\mathcal{D}(x',t',x,t)$, where $\Phi(x',t')$ is the scalar potential. Following the procedure of previous TPDI studies (Gusakov & Popov 2016; Hansen *et al*. 2020; Clod *et al*. 2024), the scalar potential of both UH waves $j \in [1, 2]$ is described using a Wentzel–Kramers–Brillouin (WKB) representation

$$\Phi_j(x,t) = \phi_j(x,t) e^{i\theta_j(x,t)}, \tag{2.14}$$

where $\phi_j(x,t)$ is the envelope and $\theta_j(x,t) = \int k_j(x)\ \mathrm{d}x - \omega_j t$ is the fast phase variation. Through classical WKB methods, the envelope equation for the wave field of UH wave 1 is obtained as (Tracy *et al*. 2014; Dodin *et al*. 2019)

$$\begin{aligned}\frac{\rho_{\mathrm{nl},1}(x,t)}{\varepsilon_0} = e^{i\theta_1(x,t)}\Bigg[& i\,\partial_t\phi_1(x,t)\partial_\omega\mathcal{D}_1(k,\omega) - i\,\partial_x\phi_1(x,t)\partial_k\mathcal{D}_1(k,\omega) \\ & - \frac{i}{2}\phi_1(x,t)\partial_x\{\partial_k\mathcal{D}_1(k,\omega)\}\Bigg],\end{aligned} \tag{2.15}$$

with $\mathcal{D}(k,\omega)$ now denoting the dispersion relation for the wave, where the subscript 1 is used as a shorthand notation for $\mathcal{D}_1 = \mathcal{D}(k,\omega)|_{k=k_1(x),\,\omega=\omega_1}$. Lastly, the nonlinear charge density $\rho_{\mathrm{nl},1}$ oscillates with (k_1, ω_1) as well. Equation (2.15) is the starting point for both the spatially averaged model and the full spatio-temporal system.

https://doi.org/10.1017/S0022377826101603 Published online by Cambridge University Press

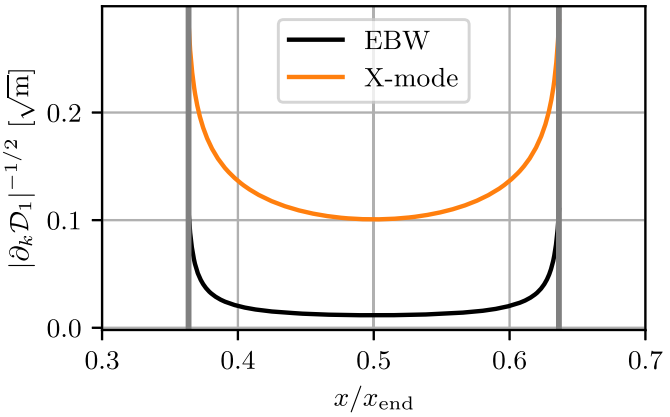


FIGURE 2. The time-independent spatial variation of the wave $\phi_1(x, t)$ for k_1 as a function of x in the plasma profile. The orange line shows the values computed for the X-mode part of the wave, and the black line is the EBW part. The grey lines show the UH layers.

2.3.1. Spatially averaged estimation

Previous estimations of TPDI growth rates assume that the spatial variation of $\phi_1(x, t)$ is constant in time (Hansen 2019; Senstius *et al*. 2022; Clod *et al*. 2024; de Wit *et al*. 2025). The assumption implies that $\phi_1(x, t)$ can be put on the form of $\phi_1(x, t) = a_1(t)b_1(x)$, where $a_1(t)$ represents a time-dependent scaling factor to the spatial profile $b_1(x)$. As in Hansen (2019), a reasonable expression for $b_1(x)$ is obtained by considering the steady-state solution to the linear part of (2.15)

$$-\partial_x \phi_1(x)\partial_k \mathcal{D}_1 - \frac{1}{2}\phi_1(x)\partial_x\left\{\partial_k \mathcal{D}_1\right\} = 0. \tag{2.16}$$

The equation is a dynamic equation dictating how the envelope of the wave evolves as it propagates in space. The solution to (2.16) is obtained as $\phi_1(x) = a_{0,1}b_1(x)$, $b_1(x) = 1/\sqrt{\partial_k \mathcal{D}_1}$, where the time-independent spatial variation is shown in figure 2 for both the EBW and X-mode part of the wave. It can be noted that they diverge at the UH layers with unphysically high values (Tracy *et al*. 2014). This results from a direct limitation of the WKB approximation, and may influence the estimated growth rates of the TPDI. However, the phase matching condition is not fulfilled close to the UH layers, causing the contributions of these regions to the total growth rate of the instability to therefore be small. We now describe each UH wave 1, 2 as a superposition of their EBW and X-mode components, sharing a time-dependent scaling factor $a_j(t)$

$$\Phi_j(x, t) = a_j(t)\left[\frac{\exp(i\theta_j^+)}{\sqrt{\partial_k \mathcal{D}_j^+}} + \frac{\exp(i\theta_j^-)}{\sqrt{\partial_k \mathcal{D}_j^-}}\right]. \tag{2.17}$$

To align with the notation of earlier TPDI studies (Hansen 2019; Clod *et al*. 2024), the superscript '+' denotes the EBW component of the UH wave, whereas '−' is

https://doi.org/10.1017/S0022377826101603 Published online by Cambridge University Press

the X-mode part. The envelope equation in (2.15) is re-obtained now with the WKB wave amplitude from (2.17). By multiplying the expression with

$$\left[\frac{\exp(-i\theta_j^+)}{\left(\sqrt{\partial_k \mathcal{D}_j^+}\right)^*} + \frac{\exp(-i\theta_j^-)}{\left(\sqrt{\partial_k \mathcal{D}_j^-}\right)^*}\right], \tag{2.18}$$

the following relation for UH wave 1 is obtained as:

$$i\,\partial_t a_1(t)\left[\frac{\partial_\omega \mathcal{D}_1^+}{|\partial_k \mathcal{D}_1^+|} + \frac{\partial_\omega \mathcal{D}_1^-}{|\partial_k \mathcal{D}_1^-|}\right] = \frac{\rho_{\mathrm{nl},1} e^{-i\theta_1^+(x,t)}}{\varepsilon_0 \left(\sqrt{\partial_k \mathcal{D}_1^+}\right)^*}, \tag{2.19}$$

where terms with fast phase variations have been neglected, as these are assumed to ultimately mix to zero. The nonlinearly induced charge density is further expressed in terms of a nonlinear susceptibility χ_{nl}, such that $\rho_{\mathrm{nl},1} = E_0 \Phi_2^* \chi_{\mathrm{nl}} \varepsilon_0$, where E_0 and Φ_2 are the WKB wave fields of the injected wave and the second UH wave, respectively. The susceptibility represents nonlinear coupling strength between the three waves, and the resulting expression in taken from Gusakov *et al*. (2019*b* and Senstius *et al*. (2022)

$$\begin{aligned}\chi_{\mathrm{nl}} = &\frac{1}{2B^{(0)}} \frac{\omega_{pe}^2 \omega_{ce}^2 \omega_0^2}{(\omega_0^2 - \omega_{ce}^2)(\bar{\omega}^2 - \omega_{ce}^2)^2} \frac{k_0 k_1 k_2}{4\omega_0} \\ &\times \left(7 + 3\frac{D_0}{S_0}\frac{\omega_0}{\omega_{ce}} - \frac{4\omega_{ce}^2}{\omega_0^2}\right),\end{aligned} \tag{2.20}$$

where $\bar{\omega} = (\omega_1 + \omega_2)/2$, and D_0 and S_0 are the difference and sum parameters for the injected wave from (2.10). The wave field $\Phi_2(x, t)$ is described similarly using (2.17), and the injected X-mode wave is given as

$$E_0(x, t) = E_0 \exp(i\theta_0), \tag{2.21}$$

where E_0 is the electric field amplitude of the pump wave, assumed here to be constant, as the wave interacts only weakly with the plasma. An average value is then calculated by integrating over the interaction region

$$i\,\partial_t a_1(t) = \mathrm{E}_0 \frac{a_2^*(t)}{\langle \partial_\omega \mathcal{D}_1 \rangle} \int_{x_l}^{x_r} \mathrm{d}x\, \frac{\chi_{\mathrm{nl}} \exp[i\Psi(x)]}{\left(\sqrt{\partial_k \mathcal{D}_1^+}\right)^* \left(\sqrt{\partial_k \mathcal{D}_2^+}\right)^*}, \tag{2.22}$$

where the exponent $\Psi(x)$ takes into account the phase mismatch caused by the inhomogeneous medium

$$\Psi(x) = \int^x \mathrm{d}x'\, [k_0(x') - k_1^+(x') - k_2^+(x')]. \tag{2.23}$$

The integration bounds, x_l and x_r, are the left and right UH layers for the innermost UH wave in figure 1, respectively. The integral represents an average gain in amplitude the daughter wave attains from the nonlinear interaction as it completes a round trip in the cavity. Finally, the value $\langle \partial\omega \mathcal{D}_1(k, \omega) \rangle$ is given as

$$\langle \partial_\omega \mathcal{D}_1 \rangle = \int_{x_l}^{x_r} \left(\frac{\partial_\omega \mathcal{D}_1^+}{|\partial_k \mathcal{D}_1^+|} + \frac{\partial_\omega \mathcal{D}_1^-}{|\partial_k \mathcal{D}_1^-|}\right) \mathrm{d}x. \tag{2.24}$$

https://doi.org/10.1017/S0022377826101603 Published online by Cambridge University Press

The evolution of $a_2(t)$ is obtained similarly to (2.22), and the system of equations can be written on the following form (Senstius *et al*. 2022; Clod *et al*. 2024):

$$i\,\partial_t a_1(t) = \xi_{1,2} a_2^*(t), \quad -i\,\partial_t a_2^*(t) = \xi_{2,1}^* a_1(t). \tag{2.25}$$

The coupled system in (2.25) may now be solved as an eigenvalue problem, yielding the growth rate of their shared exponential increase in time

$$a_j(t) = a_j(0)\exp(\gamma t), \quad \gamma = \sqrt{\xi_{1,2}\xi_{2,1}^*}, \tag{2.26}$$

for daughter wave j. The coupling coefficients are given as

$$\xi_{j,b} = \frac{\mathrm{E}_0}{\langle \partial_\omega \mathcal{D}_j \rangle} \int_{x_l}^{x_r} \mathrm{d}x \, \frac{\chi_{nl} \exp[i\Psi(x)]}{\left(\sqrt{\partial_k \mathcal{D}_j^+}\right)^* \left(\sqrt{\partial_k \mathcal{D}_b^+}\right)^*}. \tag{2.27}$$

Lastly, trapped waves must interfere constructively with themselves as they perform round trips in the cavity. Only modes whose phase attains an integer multiple of 2π after completing round trips satisfy this condition, effectively resulting in a discretised frequency spectrum of allowed eigenmodes (Senstius, Nielsen & Vann 2021). The quantisation rule is given as (Gusakov & Popov 2020)

$$\int_{x_l}^{x_r} (|k^+| - |k^-|)\, \mathrm{d}x = (2m+1)\,\pi, \tag{2.28}$$

where $m \in \mathrm{N}_0$ is the quantisation number. The added π on the right-hand side of (2.28) originates from a $\pi/2$ phase shift gained at the X-mode to EBW (or the reverse) conversion point in the profile for each individual mode, which is experienced twice during a round trip. The daughter waves of the TPDI are in this study assumed to be eigenmodes that satisfy (2.28), both with an individual mode number.

2.3.2. Full calculation

Instead of estimating only the average gain in growth during a round trip in the cavity, the envelopes $\phi_1(x,t)$ and $\phi_2(x,t)$ may be directly evolved forward in space and time. Turning to the envelope equation in (2.15), the UH waves are again described by a superposition of their EBW and X-mode components

$$\Phi_j(x,t) = \phi_j^+(x,t) e^{i\theta_j^+(x,t)} + \phi_j^-(x,t) e^{i\theta_j^-(x,t)}. \tag{2.29}$$

Isolating the time derivatives of $\phi_j(x,t)$ and neglecting terms with fast phase variations, the envelope (2.15) can be cast as two separate equations, one for the X-mode part and one for the EBW part. We start with the X-mode part that is assumed to not experience any nonlinear wave interactions. Equation (2.15) is simplified by introducing the scaled amplitude $a_j^-(x,t)$, such that

$$\phi_j^-(x,t) = \frac{a_j^-(x,t)}{\sqrt{\partial_k \mathcal{D}_j^-}}, \tag{2.30}$$

which is similar to the solution for $\phi_j(x)$ in the steady-state system in (2.16), leading to

$$\frac{i\,\partial_\omega \mathcal{D}_j^-}{\sqrt{\partial_k \mathcal{D}_j^-}} \left(\partial_t a_j^- + v_{gj}^- \partial_x a_j^-\right) = 0, \tag{2.31}$$

https://doi.org/10.1017/S0022377826101603 Published online by Cambridge University Press

where $v_{gj}^{-} = -\partial_k \mathcal{D}_j^{-} / \partial_\omega \mathcal{D}_j^{-}$ is the group velocity of the X-mode part. The nonlinear coupling term is introduced in the EBW part of the wave, yielding instead

$$\partial_t a_j^{+} = -v_{gj}^{+} \partial_x a_j^{+} + \Lambda_{j,b} a_b^{+*} e^{i\Psi(x)}, \tag{2.32}$$

where the coupling strength $\Lambda_{j,b}$ is given by

$$\Lambda_{j,b} = -i\,\mathrm{E}_0 \frac{\chi_{nl}\sqrt{\partial_k \mathcal{D}_j^{+}}}{\partial_\omega \mathcal{D}_j^{+} \left(\sqrt{\partial_k \mathcal{D}_b^{+}}\right)^{*}}. \tag{2.33}$$

Equations (2.32) and (2.31) may now be computed on a spatial grid and evolved forward in time. To ensure a linear conversion between the X-mode and EBW components for each UH wave, an *ad hoc* term is added to both expressions, defined as $w(a_j^{-} - a_j^{+})$. The parameter w is positive and only non-zero at the location where the X-mode converts into its counter-propagating EBW component. It is chosen here to be located a few grid cells before the true UH layer appears. Oppositely, the expression is only non-zero and negative at the other end, where the EBW mode converts back into the X-mode again. The phase information of the daughter wave eigenmodes is precomputed and stored in $\Psi(x)$ in the coupling term of (2.32). If both the X-mode and EBW components of the modes were to couple nonlinearly with the pump wave in the model, it is important to remember the $\pi/2$ phase shift gained at each conversion point.

Due to numerical stability, the conversion term will only raise the amplitude of the other component while not draining the corresponding incoming wave. The incoming wave instead outflows the domain located between the UH layers with a fixed and finite velocity, before reaching a damping region at the ends of the total domain. The spatial derivatives are computed using either a fourth-order finite forward or backward difference scheme, to match the sign of their velocities. The differential schemes also have periodic indexing at the boundaries, creating periodic boundary conditions for small residuals of the wave field amplitudes of order $\mathcal{O}(\epsilon)$ that remain after the damping. This is done to avoid potential oscillatory behaviours from discontinuities in the amplitude gradients. Finally, the time-dependent spatial envelope profiles are evolved forward in time using a fourth-order Runge–Kutta scheme. In the absence of a pump wave field, the UH waves propagate independently with expected group velocities and conserved amplitudes after multiple round trips in the cavity.

Both $a_1^{+}(x,t)$ and $a_2^{+}(x,t)$ are initialised on the spatial grid with baseline values and a randomised phase, while also being seeded with small-scale noise and a sinusoidal pattern to emulate potential inhomogeneities. Their X-mode counterparts have the same baseline values with only noise added. The initial conditions for $\phi_1^{+}(x,t)$ can be seen in figure 3. The wave field ϕ_2^{+} is excluded in the plot for visual clarity, but it looks similar as well.

The constant amplitude of the injected X-mode wave is defined through the intensity of a plane wave in vacuum, $\mathrm{E}_0 = \sqrt{2I_0/(c\varepsilon_0)}$, where $I_0 = 1\,\mathrm{kW\,cm^{-2}}$ is a fixed intensity. The growth rate of the instability is measured by computing the spatial mean between the UH layers of each wave, shown in figure 4. A linear fit on the form $y = 2m_1\,t + m_2$ is computed for the logarithmic values of $a_1^{+}(x,t)$, yielding $2m_1 = (2.14 \pm 0.02) \times 10^{-2}\,\mathrm{ns^{-1}}$. For comparison, the spatially averaged method estimates a growth rate of $2\gamma = 2.11 \times 10^{-2}\,\mathrm{ns^{-1}}$, which lies close in value. It is also

https://doi.org/10.1017/S0022377826101603 Published online by Cambridge University Press

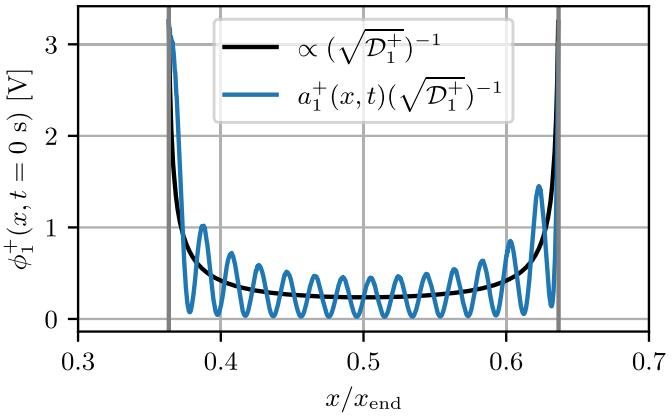


FIGURE 3. The initial profile of $\phi_1^+(x, t)$ at time $t = 0$ s, plotted as the blue line. The black line shows the profile, implied by the separation of variables for the spatially averaged model. The grey lines mark the UH layers.

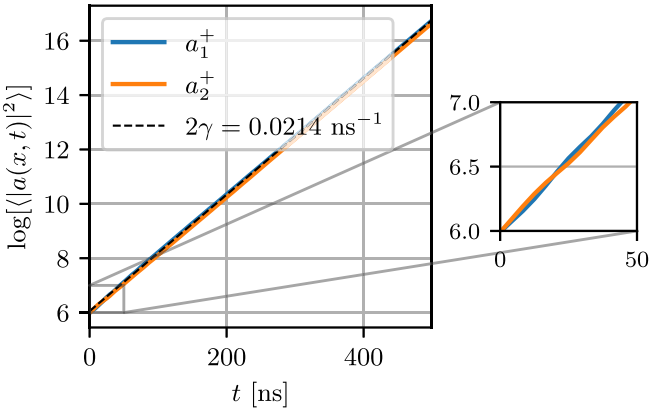


FIGURE 4. The spatial mean of the power of each wave's envelope profile plotted as a function of time in logarithmic values. The dashed black line shows the numerical fit that is computed with the measured growth rate.

noted that the growths in figure 4 fluctuate at early times ($t < 300$ ns) due to the initial inhomogeneities. A zoom-in of this is highlighted in the figure. However, after the transient period ($t > 300$ ns) their increments become steady, suggesting that the envelopes converge toward the expected form $\phi_j(x, t) = a_j(t)b_j(x)$. To further assess this, $\phi_1^+(x, t_i)$ is plotted in figure 5 at five different time instances, $t_i \in \{0, 75, 150, 225, 300\}$ ns, where the values are normalised by the exponential growth from the instability. It is seen that the instability drives ϕ_1^+ toward a smooth, steady-state profile, scaled by the exponential growth factor $\exp(\gamma t)$. In other words, noise and inhomogeneities from the initial profile are evened out, and the full solution asymptotically satisfies the separation of variables assumption. This asymptotic convergence has been further verified by applying various initial conditions for the envelopes, including cases that deviate significantly from $\propto (\sqrt{\mathcal{D}_j})^{-1}$. In all cases, similar spatial profiles of ϕ_1^+ and ϕ_2^+ were reached after approximately 300 ns.

https://doi.org/10.1017/S0022377826101603 Published online by Cambridge University Press

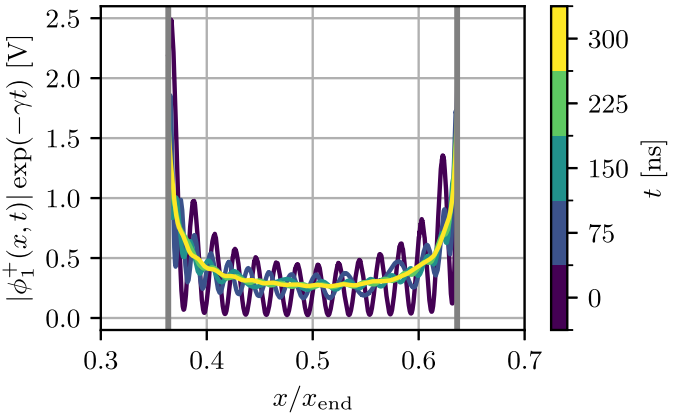


FIGURE 5. The envelope $\phi_1^+(x, t)$ plotted as a function of position for multiple times instances. The values are divided by the exponential growth $\exp(\gamma t)$.

Reducing the coupling strength by a factor of three extended the transient period to approximately 900 ns. These results imply that the spatially averaged model can be reliably applied after time scales of roughly $10/(2\gamma)$, provided that secondary decay processes have not yet impacted ϕ_1^+ and ϕ_2^+ locally within the domain.

3. Conclusion

We have investigated the validity of a spatially averaged TPDI model for estimating the exponential growth of two trapped UH waves that couple to an injected X-mode polarised wave. The model describes the UH waves by an envelope equation, derived from classical WKB methods, and assumes a separation of variables between the temporal and spatial parts of the wave fields. Based on this, the spatially averaged gain and the total growth rate in the linear regime of the instability can be computed.

To test this assumption, we directly modelled the UH waves on a spatial grid and evolved them in time using a fourth-order Runge–Kutta scheme. We found that initially imposed inhomogeneities in the field amplitudes were smoothed out by the instability, which drove the amplitudes toward a time-independent spatial profile scaled by an exponential growth factor. This relaxation occurred over a transient period of roughly 300 ns. In general, convergence to the steady-state profile was achieved after approximately $10/(2\gamma)$ ns, independent of the initial shape of the field amplitudes. An exponential fit to the UH wave growth yielded a rate of $(2.14 \pm 0.02) \times 10^{-2}\,\mathrm{ns}^{-1}$, in close agreement with the spatially averaged prediction of $2.11 \times 10^{-2}\,\mathrm{ns}^{-1}$. This demonstrates that the spatially averaged model is asymptotically valid.

In conclusion, the results show that the spatially averaged model provides an accurate estimate of the growth rate for the one-dimensional two-plasmon decay instability. The newly developed spatio-temporal method also enables modelling of additional parametric interactions with escaping waves, for instance secondary parametric saturation processes of the instability.

Acknowledgements

This work has been funded by Novo Nordisk Fonden, NNF22OC0076017, and the Carlsberg Foundation grant, CF23-0181. This work has been carried out within

https://doi.org/10.1017/S0022377826101603 Published online by Cambridge University Press

the framework of the EUROfusion Consortium, funded by the European Union via the Euratom Research and Training Programme (Grant Agreement No 101052200 -EUROfusion). Views and opinions expressed are, however, those of the author(s) only and do not necessarily reflect those of the European Union or the European Commission. Neither the European Union nor the European Commission can be held responsible for them.

Editor Paolo Ricci thanks the referees for their advice in evaluating this article.

Data availability statement

All data that support the findings of this study are included within the article (and any supplementary files).

Declaration of interests

The authors report no conflicts of interest.

REFERENCES

CLOD, A., SENSTIUS, M.G., DE WIT, J.K., SHEVCHENKO, V.F., LOPEZ, N. & NIELSEN, S.K. 2025 On perpendicularly propagating electromagnetic lower hybrid waves and ion bernstein waves in a multi-component plasma. *Phys. Plasmas* **32**, 052101.

CLOD, A., SENSTIUS, M.G., NIELSEN, A.H., RAGONA, R., THRYSØE, A.S., KUMAR, U., CODA, S. & NIELSEN, S.K. 2024 Cascades of parametric instabilities in the tokamak plasma edge during electron cyclotron resonance heating. *Phys. Rev. Lett.* **132**, 135101.

DODIN, I.Y., RUIZ, D.E., YANAGIHARA, K., ZHOU, Y. & KUBO, S. 2019 Quasioptical modeling of wave beams with and without mode conversion. I. Basic theory. *Phys. Plasmas* **26**, 072110.

GUSAKOV, E.Z. & POPOV, A.Y. 2016 Theory of anomalous backscattering in second harmonic X-mode ECRH experiments. *Phys. Plasmas* **23**, 082503.

GUSAKOV, E.Z. & POPOV, A.Y. 2020 Low-power-threshold parametric decay instabilities of powerful microwave beams in toroidal fusion devices. *Phys.-USP+* **63**, 365.

GUSAKOV, E.Z. & POPOV, A.YU 2017 Influence of the pump depletion on the anomalous absorption of the extraordinary wave in the second harmonic ecrh experiments. *Plasma Phys. Control. Fusion* **60**, 025001.

GUSAKOV, E.Z., POPOV, AYU & TRETINNIKOV, P.V. 2019*a* The possibility of anomalous gyrotron frequency sub-harmonics emission in the ecrh experiments at toroidal devices. *Nucl. Fusion* **59**, 106040.

GUSAKOV, E.Z., POPOV, A.Y. & TRETINNIKOV, P.V. 2019*b* Kinetic theory of electrostatic waves nonlinear coupling in the magnetized plasma in presence of extraordinary pump wave. *Plasma Phys. Control Fusion* **61**, 085008.

HANSEN, S.K. 2019 Parametric decay instabilities in the electron cyclotron resonance heating beams at asdex upgrade. PhD thesis, Technical University of Denmark.

HANSEN, S.K., NIELSEN, S.K., STOBER, J. & EUROfusion MST1 Team and ASDEX Upgrade Team 2023 Relativistic analysis of upper hybrid wave propagation and trapping. *Phys. Plasmas* **30**, 042103.

HANSEN, S.K., NIELSEN, S.K., STOBER, J., RASMUSSEN, J., STEJNER, M., HOELZL, M., JENSEN, T. & the ASDEX Upgrade Team 2020 Parametric decay instabilities near the second-harmonic upper hybrid resonance in fusion plasmas. *Nucl. Fusion* **60**, 106008.

NIELSEN, S.K., SALEWSKI, M., WESTERHOF, E., BONGERS, W., KORSHOLM, S.B., LEIPOLD, F., OOSTERBEEK, J.W., MOSEEV, D., STEJNER, M. & the TEXTOR Team 2013 Experimental characterization of anomalous strong scattering of mm-waves in textor plasmas with rotating islands. *Plasma Phys. Control. Fusion* **55**, 115003.

https://doi.org/10.1017/S0022377826101603 Published online by Cambridge University Press

POPOV, A.YU & GUSAKOV, E.Z. 2015 Low-threshold absolute two-plasmon decay instability in the second harmonic electron cyclotron resonance heating experiments in toroidal devices. *Plasma Phys. Control. Fusion* **57**, 025022.

SENSTIUS, M.G. *et al.* 2019 Particle-in-cell simulations of parametric decay instabilities at the upper hybrid layer of fusion plasmas to determine their primary threshold. *Plasma Phys. Control. Fusion* **62**, 25010.

SENSTIUS, M.G., FREETHY, S.J. & NIELSEN, S.K. 2024 On the selection rules for three-wave interactions along ray trajectories. *Phys. Plasmas* **31**, 032308.

SENSTIUS, M.G., GUSAKOV, E.Z., YU POPOV, A. & NIELSEN, S.K. 2022 Absolute parametric decay instabilities of x2 microwave beams in reduced models and fully kinetic codes. *Plasma Phys. Control. Fusion* **64**, 115001.

SENSTIUS, M.G., NIELSEN, S.K. & VANN, R.G.L. 2021 Trapped upper hybrid waves as eigenmodes of non-monotonic background density profiles. *Plasma Phys. Control. Fusion* **63**, 065018.

SWANSON, D.G. 2003 *Plasma Waves*. CRC Press.

TANCETTI, A. *et al.* 2022*a* Nonlinear decay of high-power microwaves into trapped modes in inhomogeneous plasma. *Nucl. Fusion* **62**, 074003.

TANCETTI, A. *et al.* 2022*b* Inhibition of parametric decay in heating microwave beams during fluctuations of the density profile in the edge island of wendelstein 7-x. *Plasma Phys. Control. Fusion* **65**, 015001.

TRACY, E.R., BRIZARD, A.J., RICHARDSON, A.S. & KAUFMAN, A.N. 2014 *Ray Tracing and Beyond: Phase Space Methods in Plasma Wave Theory*, Frontiers in Physics Series. Cambridge University Press.

WESTERHOF, E. *et al.* 2009 Strong scattering of high power millimeter waves in tokamak plasmas with tearing modes. *Phys. Rev. Lett.* **103**, 125001.

DE WIT, J.K., SENSTIUS, M.G., CLOD, A., RAGONA, R. & NIELSEN, S.K. 2025 Parametric decays into trapped microwaves in low-temperature laboratory plasmas. *Plasma Phys. Control. Fusion* **67**, 055026.

https://doi.org/10.1017/S0022377826101603 Published online by Cambridge University Press